



Selective and efficient quantum state tomography for multiqubit systems

Downloaded from: <https://research.chalmers.se>, 2026-06-15 23:32 UTC


Citation for the original published paper (version of record):

Patel, A., Gaikwad, A., Huang, T. et al (2026). Selective and efficient quantum state tomography for multiqubit systems. *Physical Review Research*, 8(1). <http://dx.doi.org/10.1103/hynl-kx12>

N.B. When citing this work, cite the original published paper.

Selective and efficient quantum state tomography for multiqubit systems

Aniket Patel , Akshay Gaikwad , Tangyou Huang , Anton Frisk Kockum , and Tahereh Abad ^{*}
Department of Microtechnology and Nanoscience, Chalmers University of Technology, 41296 Gothenburg, Sweden

 (Received 8 July 2025; revised 15 December 2025; accepted 13 February 2026; published 30 March 2026)

Quantum state tomography (QST) is a crucial tool for characterizing quantum states. However, performing full QST becomes impractical for reconstructing multiqubit density matrices since datasets and computational costs grow exponentially with qubit number. To bypass full QST, we introduce selective and efficient QST (SEEQST)—a method that enables efficient estimation of multiple selected elements of an arbitrary multiqubit density matrix. We show that any N -qubit density matrix can be partitioned into 2^N disjoint subsets, each containing 2^N elements. With SEEQST, any such subset can be accurately estimated from just two experiments with only single-qubit measurements. The complexity for estimating any subset remains constant regardless of Hilbert-space dimension, so, if desired, SEEQST can reconstruct the full density matrix, using $2^{N+1} - 1$ experiments, where standard methods would use 3^N experiments. We provide a circuit decomposition for the SEEQST experiments, demonstrating that their maximum circuit depth scales logarithmically with N assuming all-to-all connectivity.

DOI: [10.1103/hynl-kx12](https://doi.org/10.1103/hynl-kx12)

I. INTRODUCTION

Quantum state tomography (QST) reconstructs the complete density matrix of a quantum system by measuring the expectation values of observables and performing computational postprocessing [1–5]. Such characterization of quantum states is crucial for the development of quantum technologies [6–8]. However, despite its conceptual simplicity, full QST becomes impractical for large systems, since data and computational demands increase rapidly with system size [9–11].

Well-established and widely used approaches for QST include maximum-likelihood estimation (MLE) [12–17], gradient-descent algorithms [18–23], machine learning and deep neural networks [24–31], variational algorithms [32,33], convex optimization techniques [34–38], and many others [39–42]. While these methods try to speed up QST, primarily by focusing on the postprocessing step (reconstructing the full density matrix from collected data), they all suffer from the fundamental limitations of growing requirements for data and computation.

The exponential scaling of full QST with system size is an inherent characteristic of reconstructing a high-dimensional quantum state, not an artifact of existing techniques. However, there remains significant room for devising flexible and information-theoretic approaches to the data acquisition itself [43–46]. It is both realistic and efficient to perform only those experiments that yield specific partial information of

interest encoded in specific elements of the density matrix. Such strategic data collection could enable efficient partial state reconstruction, offering practical benefits and insights into quantum systems without full QST. This principle forms the foundation of the approach we introduce in this article.

Recent approaches to estimating selected elements of density matrices have primarily relied on weak measurements (WMs) [47–53]. While WMs enable direct extraction of specific density-matrix elements without complex data postprocessing, they require pure ancilla qubits and complex multiqubit entangling operations, making them resource-intensive and challenging to implement [49,50]. Additionally, WM strategies are inherently approximate and suffer from a trade-off: Validity of the approximation necessitates weaker interactions, while reducing statistical uncertainties requires stronger ones.

Beyond WM schemes, few alternative protocols have been developed [54–62]. Phase-shifting schemes [54,55] can estimate a single density-matrix element of a multiqubit system using only six expectation values. In Ref. [56], a fixed controlled-swap network was used to compute density-matrix functionals, requiring ancilla qubits. Selective QST has also been explored for both discrete- and continuous-variable systems, where precision depends on the number of experiments [57,59,61,63]. Additionally, hardware-specific direct measurement techniques have been used to reconstruct quantum state coefficients of a 10^5 -dimensional entangled state in an optical setup [58], as well as methods based on stimulated Raman adiabatic passage [64]. A recently reported partial quantum shadow tomography scheme [65] enables the estimation of a subset of density-matrix elements. Other works explore experimental requirements for pure state tomography; however, they inherently lack selectivity [66,67]. Despite these advances, a universal, scalable approach for selectively estimating density-matrix elements remains elusive.

^{*}Contact author: tahereh.abad@chalmers.se

Published by the American Physical Society under the terms of the Creative Commons Attribution 4.0 International license. Further distribution of this work must maintain attribution to the author(s) and the published article's title, journal citation, and DOI. Funded by Bibsam.

Existing protocols are often constrained by specific hardware requirements, system size, accuracy, and precision, scaling unfavorably with Hilbert-space dimension.

In this article, we address this fundamental challenge by introducing selective and efficient quantum state tomography (SEEQST). Using only two carefully designed experiments, SEEQST enables efficient estimation of specific density-matrix elements. Here, *efficient* is with respect to the number of experimental settings required, not the data-processing algorithm that computes the elements. We demonstrate that an N -qubit density matrix can be systematically partitioned into 2^N disjoint subsets, each containing a predefined set of 2^N elements, and that any chosen subset can be accurately estimated using our SEEQST protocol without requiring complex, nonlinear data-processing algorithms that enforce physical validity constraints. Such validity constraints are only relevant for reconstruction of the full density matrix, not for selectively estimating targeted elements. Notably, SEEQST maintains constant complexity per subset, independent of Hilbert-space dimension, making it highly scalable for multiqubit systems. We provide a circuit decomposition for SEEQST, showing that its maximum circuit depth scales logarithmically with the number of qubits for all-to-all connectivity.

Most traditional data-acquisition experiments for QST are either derived from Pauli partitioning [68,69] or naive local rotation operations, e.g., $\{I, R_x, R_y\}^{\otimes N}$. Such methods do not allow selective partial reconstruction of the underlying density matrix and require processing of entire dataset at once to reconstruct the quantum state. In contrast, SEEQST enables not only estimation of selective elements, but also independent and parallel subset computation for faster full QST, if desired. This significantly reduces computational overhead and enhances scalability, establishing SEEQST as a powerful alternative to conventional QST data-acquisition techniques.

We provide a Python code to implement our SEEQST [70] protocol. The first part of the code takes a list of targeted density-matrix elements as input and outputs the required experiments. The second part uses the data from these proposed experiments as input to estimate the elements. Our code also includes a version of SEEQST based on only local operations.

II. SELECTIVE AND EFFICIENT QUANTUM STATE TOMOGRAPHY PROTOCOL

An N -qubit density matrix ρ has elements

$$\rho_{ij} = \langle i|\rho|j\rangle, \quad (1)$$

where $\{|i\rangle\}$ are the computational basis vectors; $i \in [0, 1, \dots, 2^N - 1]$, such that ρ_{ij} corresponds to the element in the $(i + 1)$ th row and $(j + 1)$ th column. To compute ρ_{ij} , one must evaluate the expectation value of the operator

$$\Pi_{ij} = |j\rangle\langle i|. \quad (2)$$

In general, Π_{ij} is a non-Hermitian operator, except when $i = j$, which yields diagonal elements. This underscores the challenge of selectively estimating off-diagonal elements of ρ . A straightforward approach is to express Π_{ij} as

$$\sum_m a_m^{ij} E_m, \quad (3)$$

where a_m^{ij} are complex coefficients and $\{E_m\}$ are Hermitian operators forming a basis, typically the N -qubit Pauli set:

$$E_m \in \{I, \sigma_x, \sigma_y, \sigma_z\}^{\otimes N}. \quad (4)$$

Measuring $\langle E_m \rangle$ for nonzero a_m^{ij} then allows estimation of $\langle \Pi_{ij} \rangle$ via $\sum_m a_m^{ij} \langle E_m \rangle$. This approach requires fewer experiments than full QST, but the number still scales exponentially with the number of qubits, due to the lack of a well-defined link between target elements and the required measurements [71,72].

With SEEQST, we provide a more efficient strategy to first determine the optimal Pauli-operator set corresponding to the targeted elements and then collectively compute these operators instead of measuring them individually, effectively minimizing the number of required experiments. We first illustrate how this works for single- and two-qubit systems, before generalizing to N qubits.

A. Single-qubit case

In single-qubit SEEQST, the 2×2 density matrix is partitioned into two disjoint sets:

$$S_1 = \{\rho_{00}, \rho_{11}\} \quad (\text{diagonal elements, } i = j), \quad (5)$$

$$S_2 = \{\rho_{01}, \rho_{10}\} \quad (\text{off-diagonal elements, } i \neq j). \quad (6)$$

The elements of S_1 are determined by measuring $\{I, \sigma_z\}$; those in S_2 are estimated using $\{\sigma_x, \sigma_y\}$. Here, the identity operator I is redundant, as its expectation value is always 1, so S_1 can be determined in a single experiment by just measuring σ_z . In contrast, estimating S_2 requires two separate experiments, one for measuring σ_x and another for σ_y , since $[\sigma_x, \sigma_y] \neq 0$. Thus, for a single qubit, SEEQST is essentially equivalent to the standard measurement scheme based on $\{I, R_x, R_y\}$ for full QST. However, this equivalence does not hold for multiqubit systems, as demonstrated next.

B. Two-qubit case

For two-qubit SEEQST, the density-matrix elements are

$$\rho_{ij} = \rho_{i_1 i_2, j_1 j_2} = \langle i_1 i_2 | \rho | j_1 j_2 \rangle, \quad (7)$$

where $i_1 i_2$ and $j_1 j_2$ are binary representations of i and j , respectively, labeling the two-qubit computational basis states. The 4×4 density matrix can be partitioned into four disjoint sets with four elements each, $\{S_1, S_2, S_3, S_4\}$, represented by different colors in Fig. 1, based on whether the indices corresponding to each qubit, i.e., i_1 and j_1 (or i_2 and j_2), are identical or not. Specifically,

$$S_1 = \{\rho_{i_1 i_2, j_1 j_2} | i_1 = j_1, i_2 = j_2\} \quad (8)$$

consists of all diagonal elements (yellow in Fig. 1), while

$$S_2 = \{\rho_{i_1 i_2, j_1 j_2} | i_1 = j_1, i_2 \neq j_2\} \quad (9)$$

has the elements that are diagonal in the first qubit but off-diagonal in the second (blue in Fig. 1). Similarly,

$$S_3 = \{\rho_{i_1 i_2, j_1 j_2} | i_1 \neq j_1, i_2 = j_2\}, \quad (10)$$

$$S_4 = \{\rho_{i_1 i_2, j_1 j_2} | i_1 \neq j_1, i_2 \neq j_2\} \quad (11)$$

(green and red, respectively, in Fig. 1). The elements in any set can thus be obtained from a single element by preserving

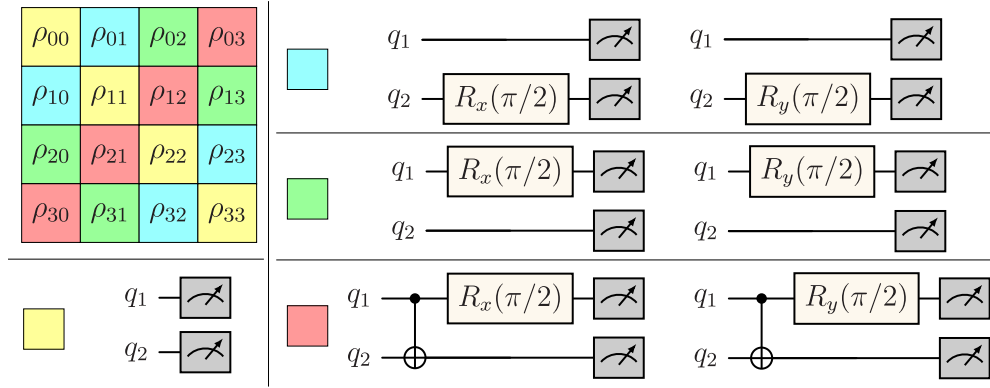


FIG. 1. Classification of two-qubit density-matrix elements based on the parity-preserving structure of indices required for SEEQST. Each class is represented by a color (yellow, blue, green, or red) and two corresponding quantum circuits for measurements determining all density-matrix elements in the class (one experiment for the diagonal elements).

the parities of the pairs of indices (i_1, j_1) and (i_2, j_2) through the transformation

$$\{I, X\}^{\otimes 2}(i_1 i_2, j_1 j_2) \rightarrow (i'_1 i'_2, j'_1 j'_2), \quad (12)$$

where X denotes a bit-flip gate and the first (second) operator acts on both i_1 (i_2) and j_1 (j_2).

This partitioning of the density-matrix elements into sets provides a systematic framework for reconstructing ρ and selectively estimating desired elements $\rho_{i_1 i_2, j_1 j_2}$. The partitioning reflects the decomposition of ρ in the Pauli operator basis: Diagonal elements ($i_{1(2)} = j_{1(2)}$) correspond to $\{I, \sigma_z\}$, while off-diagonal elements ($i_{1(2)} \neq j_{1(2)}$) are associated with $\{\sigma_x, \sigma_y\}$. Hence, the optimal observables for each set are

$$\Pi^{S_1} = \{I, \sigma_z\} \otimes \{I, \sigma_z\}, \quad (13)$$

$$\Pi^{S_2} = \{I, \sigma_z\} \otimes \{\sigma_x, \sigma_y\}, \quad (14)$$

$$\Pi^{S_3} = \{\sigma_x, \sigma_y\} \otimes \{I, \sigma_z\}, \quad (15)$$

$$\Pi^{S_4} = \{\sigma_x, \sigma_y\} \otimes \{\sigma_x, \sigma_y\}. \quad (16)$$

Together, these sets span all 16 Pauli matrices, forming a tomographically complete set if full QST is desired.

We now demonstrate that just two measurement settings are sufficient to determine any entire set S_k . For instance,

$$\Pi^{S_3} = \{\sigma_x \otimes I, \sigma_x \otimes \sigma_z, \sigma_y \otimes I, \sigma_y \otimes \sigma_z\} \quad (17)$$

can be divided into two subsets of mutually commuting observables:

$$\mathcal{E}(\Pi^{S_3}) = \{\sigma_x \otimes I, \sigma_x \otimes \sigma_z\}, \quad (18)$$

$$\mathcal{O}(\Pi^{S_3}) = \{\sigma_y \otimes I, \sigma_y \otimes \sigma_z\}. \quad (19)$$

Each subset corresponds to a distinct measurement setting in the common eigenbasis of $\mathcal{E}(\Pi^{S_3})$ and $\mathcal{O}(\Pi^{S_3})$. The required quantum circuits are easily constructed by implementing basis transformations associated with $\mathcal{E}(\Pi^{S_3})$ and $\mathcal{O}(\Pi^{S_3})$, utilizing their normalized common eigenstates,

$$\mathcal{E}(\Pi^{S_3}): |e_q^\pm\rangle = \frac{1}{\sqrt{2}}(|0\rangle \pm |1\rangle)|q\rangle, \quad (20)$$

$$\mathcal{O}(\Pi^{S_3}): |o_q^\pm\rangle = \frac{1}{\sqrt{2}}(|0\rangle \pm i|1\rangle)|q\rangle, \quad (21)$$

where $q \in \{|0\rangle, |1\rangle\}$, followed by standard measurements in the computational basis. The basis transformations for $\mathcal{E}(\Pi^{S_3})$ and $\mathcal{O}(\Pi^{S_3})$ are

$$U_{\mathcal{E}} = [|e_0^+\rangle \quad |e_0^-\rangle \quad |e_1^+\rangle \quad |e_1^-\rangle]^\dagger, \quad (22)$$

$$U_{\mathcal{O}} = [|o_0^+\rangle \quad |o_0^-\rangle \quad |o_1^+\rangle \quad |o_1^-\rangle]^\dagger. \quad (23)$$

Alternative transformations can be obtained by permuting columns within $U_{\mathcal{E}}$ and $U_{\mathcal{O}}$. However, in this particular case, the unitary operators decompose into local operations,

$$U_{\mathcal{E}} = R_y(\pi/2) \otimes I, \quad (24)$$

$$U_{\mathcal{O}} = R_x(\pi/2) \otimes I, \quad (25)$$

simplifying implementation. A similar approach applies to S_1 , S_2 , and S_4 . For the diagonal elements (S_1), only a single experiment is needed, as all observables in the corresponding set mutually commute. For S_4 , both experiments involve a controlled-NOT (CNOT) gate, resulting in the maximum circuit depth.

C. N -qubit generalization

In N -qubit SEEQST, the density-matrix elements are

$$\rho_{ij} = \langle i_1 i_2 \cdots i_N | \rho | j_1 j_2 \cdots j_N \rangle, \quad (26)$$

where $i_1 i_2 \cdots i_N$ and $j_1 j_2 \cdots j_N$ are the binary expansions of i and j , respectively. The $2^N \times 2^N$ density matrix can be systematically partitioned into 2^N sets with 2^N elements each, $\{S_1, S_2, \dots, S_{2^N}\}$, based on whether $i_l = j_l$ or $i_l \neq j_l$ for each qubit index l . Each set S_k is spanned by any single element within it through the transformations

$$\begin{aligned} \{I, X\}^{\otimes N}(i_1 i_2 \cdots i_N, j_1 j_2 \cdots j_N) \\ \rightarrow (i'_1 i'_2 \cdots i'_N, j'_1 j'_2 \cdots j'_N) \end{aligned} \quad (27)$$

that preserve the parities for each pair of indices (i_l, j_l) .

For a given set S_k , the optimal set of N -qubit Pauli observables that contribute nontrivially is

$$\Pi^{S_k} = \bigotimes_{l=1}^N \begin{cases} \{I, \sigma_z\}, & \text{if } (i_l, j_l) \in \{(0, 0), (1, 1)\}, \\ \{\sigma_x, \sigma_y\}, & \text{if } (i_l, j_l) \in \{(0, 1), (1, 0)\}. \end{cases} \quad (28)$$

In the trivial case of diagonal elements,

$$S_1 = \{\rho_{i,j} | i = j \forall l\}, \quad (29)$$

the associated set of observables,

$$\Pi^{S_1} = \{I, \sigma_z\}^{\otimes N}, \quad (30)$$

consists of mutually commuting operators. Consequently, all elements in S_1 can be determined in a single experiment: a standard measurement in the computational basis. On the other hand, the set of observables Π^{S_k} for an S_k with some off-diagonal elements, where M qubits satisfy $i_l \neq j_l$ and the remaining $N - M$ qubits have $i_l = j_l$, can be divided into two subsets of mutually commuting observables, $\mathcal{E}(\Pi^{S_k})$ and $\mathcal{O}(\Pi^{S_k})$. Specifically, $\mathcal{E}(\Pi^{S_k})$ contains Pauli tensor products with an even number of σ_y , while $\mathcal{O}(\Pi^{S_k})$ includes those with an odd number of σ_y . This division ensures that all observables within each set can be measured in a single experiment. We provide a formal proof of this statement in Appendix A. It is important to note that SEEQST is fundamentally different from standard Pauli partitioning. This distinction is described in detail in Appendix C.

Relabeling the M qubits with $i_l \neq j_l$ as the first qubits and the other $N - M$ qubits as the last, the simultaneous eigenstates of $\mathcal{E}(\Pi^{S_k})$ and $\mathcal{O}(\Pi^{S_k})$ can be expressed as

$$\mathcal{E}(\Pi^{S_k}) : |e_{p\bar{p}q}^\pm\rangle = \frac{1}{\sqrt{2}}(|p\rangle \pm |\bar{p}\rangle)|q\rangle, \quad (31)$$

$$\mathcal{O}(\Pi^{S_k}) : |o_{p\bar{p}q}^\pm\rangle = \frac{1}{\sqrt{2}}(|p\rangle \pm i|\bar{p}\rangle)|q\rangle, \quad (32)$$

where $|p\rangle \in |0\rangle \otimes \{|0\rangle, |1\rangle\}^{\otimes(M-1)}$, $|\bar{p}\rangle$ is its bitwise complement, and $|q\rangle \in \{|0\rangle, |1\rangle\}^{\otimes(N-M)}$. Although $|p\rangle \in \{|0\rangle, |1\rangle\}^{\otimes M}$ also is a valid set of eigenstates, this choice leads to redundancy; to avoid repeated eigenstates, we must fix one of the qubits to either $|0\rangle$ or $|1\rangle$.

The basis transformations $U_{\mathcal{E}}$ and $U_{\mathcal{O}}$ map the computational basis to Greenberger-Horne-Zeilinger (GHZ)-type [73,74] eigenstates as shown in Eqs. (31) and (32). These transformations are thus the conjugate transpose of the unitary operations U_{GHZ} used to prepare M -qubit GHZ states. The potential advantage of measurements in a GHZ-type entangled basis has been demonstrated in the context of reducing the sample complexity for learning Pauli expectation values [75]. These operations consist of a local rotation $R_{x(y)}(\pi/2)$ on one qubit, followed by $M - 1$ CNOT gates, as illustrated in Fig. 2, giving a maximum circuit depth that grows linearly with the number of qubits. However, the circuit depth can be reduced to $O(\log M)$ for all-to-all qubit connectivity by parallelizing the CNOT gates [76–79], as explained in Appendix E. Without entangling gates, SEEQST reduces to a constrained version of a standard measurement scheme for QST, requiring 3^N circuits for estimating the full density matrix (see Appendix G).

D. Data-processing algorithm

Typically, conventional QST experiments employ local unitary operations $\{I, R_x(\pi/2), R_y(\pi/2)\}^{\otimes N}$ for data acquisition. Except in the single-qubit case, such experiments do not permit selective reconstruction of individual density-matrix elements; instead, they require collective postprocessing to in-

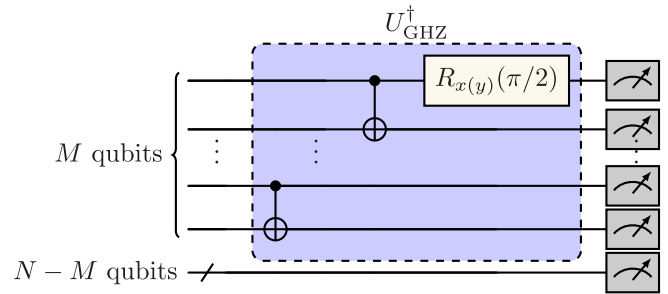


FIG. 2. Quantum circuits to implement N -qubit SEEQST. Choosing $R_x(\pi/2)$ or $R_y(\pi/2)$ in the depicted circuit implements the basis transformation $U_{\mathcal{O}}$ or $U_{\mathcal{E}}$, respectively. The first M qubits having $i_l \neq j_l$ (off-diagonal case) are acted upon by U_{GHZ}^\dagger (light purple shading). The remaining $N - M$ qubits, represented by a multiqubit quantum register with ‘/’, correspond to $i_l = j_l$ (diagonal case).

fer the full or partial density matrix. We refer to this procedure as *standard* QST.

For the data postprocessing in both standard QST and SEEQST, we employ a stochastic gradient-descent (SGD) algorithm to minimize the loss function [12,13,22]

$$\mathcal{L}(\rho_{\text{ML}}|\mathbf{d}) = - \sum_i d_i \ln(p_i), \quad (33)$$

where d_i denotes measured data from the dataset \mathbf{d} and $p_i = \text{Tr}(\Pi_i \rho_{\text{ML}})$ is the corresponding predicted data with Π_i the associated measurement operator and ρ_{ML} the predicted density matrix. In standard QST, the data \mathbf{d} are acquired using 3^N quantum circuits; in SEEQST, data are obtained from only two quantum circuits per set S_k for estimating selective elements ($2^{N+1} - 1$ circuits for the full ρ_{ML}). To restrict the optimization in the constrained space of valid quantum states, we employ a Cholesky-decomposition parametrization [12,13]:

$$\rho_{\text{ML}} = T^\dagger T / \text{Tr}(T^\dagger T), \quad (34)$$

where $T \in \mathbb{C}^{2^N \times 2^N}$. We emphasize that, even though the optimization is carried out in full density-matrix space, ρ_{ML} , we only retrieve the targeted density-matrix elements from the solution we obtain after solving Eq. (33); these elements can then be put together if full QST is desired. The validity constraints associated with the full density matrix reconstructed via SEEQST protocol are discussed in Appendix B. It should be noted that our emphasis for SEEQST is on the data-acquisition stage rather than the data-processing step.

III. RESULT AND ANALYSIS

We demonstrate the SEEQST technique on IBM quantum hardware. We conduct experiments on the *ibm_marrakesh* [80] quantum processor for two-, three-, four-, and five-qubit states. This device has a two-qubit gate error of $\sim 3.5 \times 10^{-3}$, median relaxation time $T_1 = 200 \mu\text{s}$, and median coherence time $T_2 = 115 \mu\text{s}$. Since the device does not natively support CNOT gates, we decompose those gates into a controlled-Z (CZ) gate and single-qubit operations. Due to qubit connectivity constraints on the device, extra SWAP operations are required to apply a CZ gate between desired qubits. Each SWAP

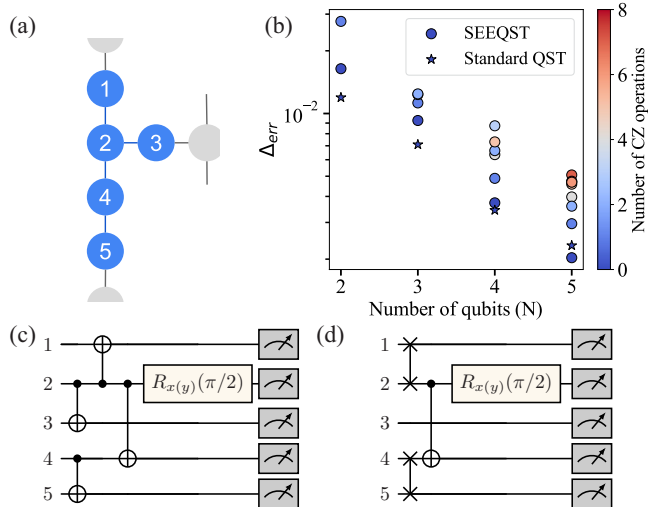


FIG. 3. Experimental implementation. (a) Layout of the five qubits used on the *ibm_marrakesh* quantum processor. (b) Average reconstruction error Δ_{err} for the state $|+\rangle^{\otimes N}$, as a function of the number of qubits N and the number of CZ operations in the SEEQST circuits. (c) The two circuits for the selective block S_{32} in a five-qubit state, where all qubits are off-diagonal. (d) The two quantum circuits for the selective block S_{18} in a five-qubit state, where q_1 and q_5 are off-diagonal. Since they are not directly connected, two additional SWAP operations are required to effectively implement CNOT_{15} as required by SEEQST.

operation, in turn, introduces three additional CZ gates, further impacting circuit depth and fidelity.

In Fig. 3, we present results from applying both standard QST and SEEQST to the $|+\rangle^{\otimes N}$ state for systems of up to $N = 5$ qubits. We chose this state as a good test case because its density-matrix elements are all nonzero, and some of them are complex. In Fig. 3(b), we show the average error in estimating an element, considering groups of elements $\cup_q S_q$ requiring the same number of CNOT operations in the SEEQST circuits:

$$\Delta_{\text{err}} = \left\langle \left| \rho_k - \rho_k^{\text{ideal}} \right| \right\rangle_{\rho_k \in \cup_q S_q}. \quad (35)$$

For instance, in the two-qubit case (see Fig. 1), Δ_{err} for no CNOT operations is computed over $\cup_q S_q = S_1 \cup S_2 \cup S_3$, while Δ_{err} for one CNOT operation is calculated using the four elements in the set S_4 .

We see in Fig. 3(b) that Δ_{err} initially decreases exponentially with the number of qubits, as the size of each matrix element becomes exponentially smaller. However, the error increases with the number of CZ operations required in the SEEQST circuits. This trend breaks down for N -qubit GHZ states (see Appendix D), where the dominant source of error is imperfections in the preparation of such an entangled state. For elements where no CZ gates are involved, the SEEQST circuit resembles standard QST, and the corresponding error closely matches that of standard QST. Thus, the error reflects a trade-off between element size and gate-induced noise.

Despite the presence of additional gate errors in SEEQST circuits, the method offers a significant advantage over standard QST in run-time. Specifically, SEEQST completes a full five-qubit QST in just 4.5 min, compared to 17.5 min for

TABLE I. State fidelity between standard QST, SEEQST, and ideal states for $|+\rangle^{\otimes N}$.

QST comparison \ $N =$	2	3	4	5
Standard and ideal	0.992	0.988	0.980	0.974
SEEQST and ideal	0.985	0.977	0.970	0.952
Standard and SEEQST	0.989	0.995	0.992	0.986

standard QST. This illustrates a practical trade-off: For many applications, the marginal increase in error from SEEQST may be acceptable, especially since standard QST already contains inherent noise. Thus, SEEQST can greatly reduce experimental overhead while still yielding high-fidelity state estimates. We further support this conclusion in Appendix H through numerical simulations of SEEQST on full-rank five-qubit states.

While Δ_{err} [see Eq. (35)] provides an intuitive sense of how circuit complexity affects estimation accuracy, it does not fully capture the impact on overall state reconstruction. Therefore, we compare full state fidelities in Table I for the experiments that we plotted Δ_{err} for in Fig. 3(b). The state fidelity is calculated as [81]

$$F(\rho, \sigma) = (\text{tr} \sqrt{\sqrt{\rho} \sigma \sqrt{\rho}})^2. \quad (36)$$

Considering the dominant readout error of approximately 1% per qubit, standard QST itself produces a noisy estimate of the quantum state. The table demonstrates that the reconstructed states from both standard QST and SEEQST are nearly identical, with fidelities ranging between 98.2% and 99.2%.

IV. CONCLUSION

We have developed a general method, SEEQST, for selective quantum state tomography of specific sets of 2^N elements within an N -qubit density matrix. This method requires only two quantum circuits per set, each employing (depending upon the set) at most $N - 1$ CNOT gates and one single-qubit rotation. As we have demonstrated both analytically and in experiments with up to $N = 5$ qubits, SEEQST enables efficient determination of specific sets of elements without the need for full tomography, and it can perform full QST using only $2^{N+1} - 1$ circuits, fewer than the 3^N circuits in standard QST. Furthermore, instead of processing the entire dataset at once to infer the quantum state, as standard QST does, SEEQST enables independent computation of subsets, facilitating parallel and simultaneous estimation for even faster full reconstruction. To enable easy implementation, we have made our SEEQST code freely accessible [70].

A possible extension of SEEQST is integration with threshold-based tomography methods [82]. In such methods, one measures the diagonal elements ρ_{ii} and use these to set a significance threshold t . This threshold provides a data-driven criterion to reduce the subsequent measurement process: The two SEEQST experiments for a subset S_k are performed only if $\sqrt{\rho_{ii} \rho_{jj}} \geq t$, meaning that at least one of its elements ρ_{ij} is predicted to be non-negligible. This reduces experimental overhead without any *a priori* assumptions on the state's structure.

Beyond applying SEEQST to speed up full QST in existing systems, future work can also extend the SEEQST framework to enable selective and efficient quantum process tomography (SEEQPT) by leveraging the state-channel duality theorem [83–85]. However, this straightforward extension would require an equal number of ancilla and system qubits. Performing SEEQPT with a variable number of ancilla qubits—or even without ancilla qubits—poses a nontrivial challenge to be explored in both discrete- and continuous-variable quantum systems. Such protocols would be valuable for efficiently extracting specific information about an unknown quantum process and diagnosing experimental quantum gates to enhance their quality, all without the need for full QPT.

ACKNOWLEDGMENTS

We thank the WACQT Quantum Technology Testbed operated by Chalmers Next Labs for help with access to IBM quantum hardware. We acknowledge support from the Knut and Alice Wallenberg Foundation through the Wallenberg Centre for Quantum Technology (WACQT) and from the Horizon Europe program HORIZON-CL4-2022-QUANTUM-01-SGA via Project No. 101113946 OpenSuperQPlus100. A.F.K. was also supported by the Swedish Foundation for Strategic Research (Grants No. FFL21-0279 and No. FUS21-0063).

DATA AVAILABILITY

The data that support the findings of this article are openly available [70].

APPENDIX A: MATHEMATICAL INDUCTION FOR TWO EXPERIMENTAL SETS

Here, we show in more detail how the set Π^{S_k} can be partitioned into two subsets of mutually commuting observables, denoted by $\mathcal{E}(\Pi^{S_k})$ and $\mathcal{O}(\Pi^{S_k})$.

We follow the convention that the M qubits for which $i_l \neq j_l$ are relabeled as the first M qubits, with the remaining $N - M$ qubits labeled as the last ones. Therefore, only σ_x or σ_y appear on the first M qubits. The corresponding observables on the first M qubits are denoted by \mathcal{E}_M and \mathcal{O}_M , representing $\mathcal{E}(\Pi^{S_k})$ and $\mathcal{O}(\Pi^{S_k})$, respectively. We now prove by induction that (1) the elements within \mathcal{E}_M commute, (2) the elements within \mathcal{O}_M commute, and (3) every element of \mathcal{E}_M anticommutes with every element of \mathcal{O}_M .

We start with the simplest case, $M = 1$, where

$$\mathcal{E}_1 = \{\sigma_x\}, \quad \mathcal{O}_1 = \{\sigma_y\}. \quad (\text{A1})$$

Here, (1) and (2) are trivially fulfilled, and (3) holds since $\{\sigma_x, \sigma_y\} = 0$.

For $M = 2$, we have

$$\mathcal{E}_2 = \{\sigma_x \otimes \sigma_x, \sigma_y \otimes \sigma_y\}, \quad \mathcal{O}_2 = \{\sigma_x \otimes \sigma_y, \sigma_y \otimes \sigma_x\}. \quad (\text{A2})$$

A straightforward calculation shows that elements within \mathcal{E}_2 commute, elements within \mathcal{O}_2 commute, and any element from \mathcal{E}_2 anticommutes with any element from \mathcal{O}_2 .

We now assume that for $M - 1$ qubits, the following holds:

$$[E_i, E_j] = 0 \quad \forall E_i, E_j \in \mathcal{E}_{M-1}, \quad (\text{A3})$$

$$[O_i, O_j] = 0 \quad \forall O_i, O_j \in \mathcal{O}_{M-1}, \quad (\text{A4})$$

$$\{E_i, O_j\} = 0 \quad \forall E_i \in \mathcal{E}_{M-1}, O_j \in \mathcal{O}_{M-1}. \quad (\text{A5})$$

We then define

$$\mathcal{E}_M = (\mathcal{E}_{M-1} \otimes \sigma_x) \cup (\mathcal{O}_{M-1} \otimes \sigma_y), \quad (\text{A6})$$

$$\mathcal{O}_M = (\mathcal{O}_{M-1} \otimes \sigma_x) \cup (\mathcal{E}_{M-1} \otimes \sigma_y). \quad (\text{A7})$$

Then, for any $E_i, E_j \in \mathcal{E}_{M-1}$, we have

$$[E_i \otimes \sigma_x, E_j \otimes \sigma_x] = [E_i, E_j] \otimes I = 0. \quad (\text{A8})$$

Similarly, for any $O_i, O_j \in \mathcal{O}_{M-1}$,

$$[O_i \otimes \sigma_y, O_j \otimes \sigma_y] = [O_i, O_j] \otimes I = 0. \quad (\text{A9})$$

For cross terms, we have

$$[E_i \otimes \sigma_x, O_j \otimes \sigma_y] = E_i O_j \otimes (\sigma_x \sigma_y) - O_j E_i \otimes (\sigma_y \sigma_x) = 0 \quad (\text{A10})$$

and

$$\{E_i \otimes \sigma_x, O_j \otimes \sigma_x\} = \{E_i, O_j\} \otimes I = 0. \quad (\text{A11})$$

Thus, the required commutation and anticommutation properties are preserved going from $M - 1$ to M , and hold for any M by induction. Finally, extending the result to N qubits by tensoring with $\{\sigma_0, \sigma_z\}^{\otimes(N-M)}$ preserves the commutation relations, since $[\sigma_0, \sigma_z] = 0$. This concludes the proof.

APPENDIX B: FULL RECONSTRUCTION AND VALIDITY CONSTRAINTS IN SEEQST

It is important to emphasize that the SEEQST protocol primarily focuses on optimizing the experimental design, i.e., generating the most efficient sets of measurements to extract selected density-matrix elements or perform targeted partial reconstructions. SEEQST itself does not introduce any new data-processing algorithm for this purpose. Rather, it serves as a flexible data-acquisition framework that is fully compatible with existing postprocessing techniques, including maximum-likelihood estimation, convex optimization, compressed sensing, and machine-learning-based reconstruction methods.

However, when full QST is desired, simultaneous block-wise reconstruction of the entire density matrix using SEEQST does not, on its own, guarantee a physically valid result. Within the SEEQST framework, only two properties are inherently satisfied: unit trace and Hermiticity. To additionally enforce the positive semidefinite (PSD) condition required for a valid quantum state, a convex projection must be applied to the initial unconstrained estimate, projecting it onto the PSD space, as also demonstrated in, e.g., Refs. [19,72,86–88], with the constrained optimization problem

$$\begin{aligned} \min_{\rho_{\text{phys}}} \quad & \|\rho_{\text{phys}} - \rho_{\text{SEEQST}}\|_F \\ \text{s.t.} \quad & \rho_{\text{phys}} \succeq 0, \\ & \text{Tr}(\rho_{\text{phys}}) = 1, \end{aligned}$$

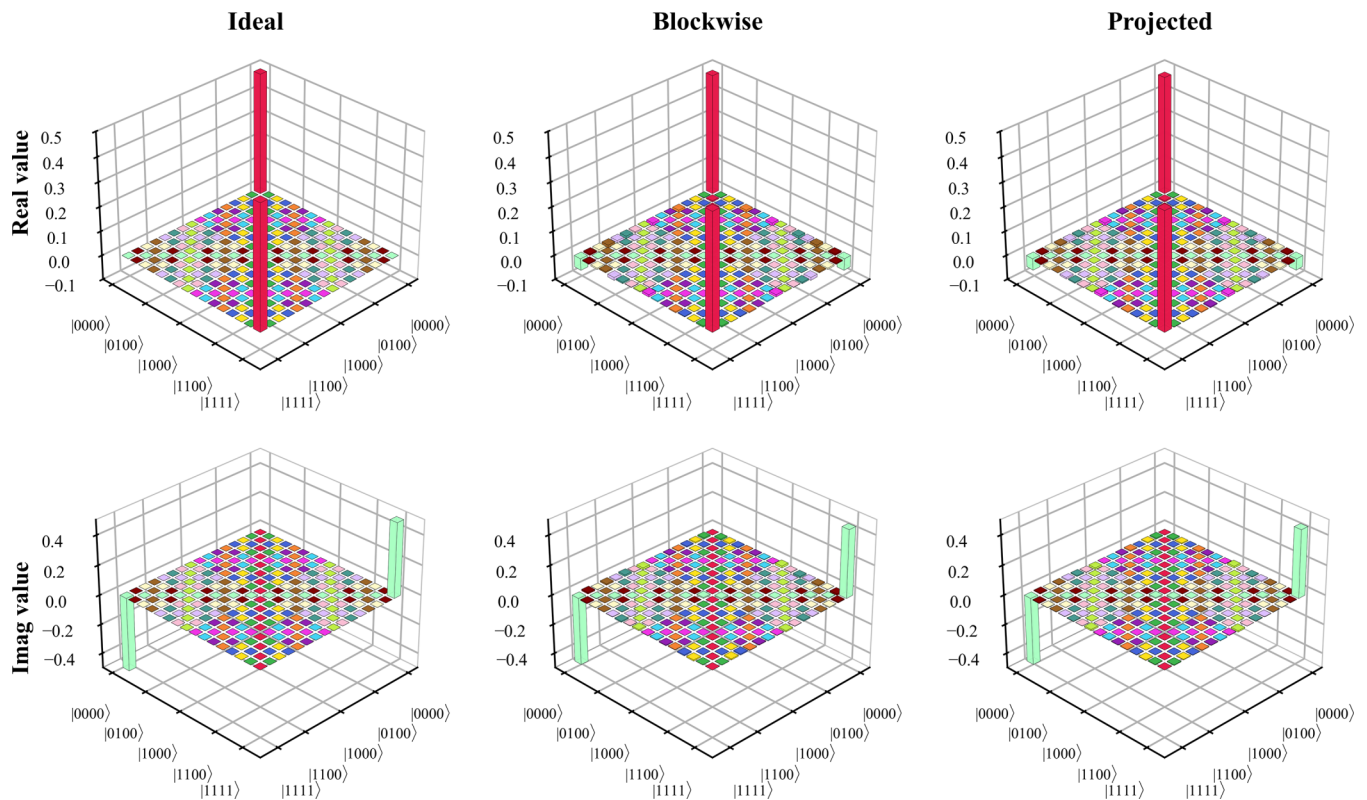


FIG. 4. Full reconstruction of the GHZ state $(|0000\rangle - i|1111\rangle)/\sqrt{2}$ using the SEEQST protocol. The first column shows the ideal density matrix, while the second and third columns display the unconstrained blockwise reconstruction obtained via SEEQST and the PSD-projected (physically valid) density matrix, respectively. The top and bottom rows correspond to the real and imaginary parts of the density matrix. Different colors indicate the distinct partition subsets S_k .

where $\|\cdot\|_F$ represents the Frobenius norm of a matrix. The variable matrix ρ_{phys} is the physically valid density matrix obtained after optimization and ρ_{SEEQST} represents the unconstrained estimate of the full density matrix obtained using the SEEQST method, i.e., by minimizing Eq. (33) for all subsets S_k .

As a demonstration, Fig. 4 presents the experimental tomographic results for both the unconstrained SEEQST reconstruction (ρ_{SEEQST}) and the corresponding PSD-projected physical density matrix (ρ_{phys}) of a four-qubit GHZ state, $(|0000\rangle - i|1111\rangle)/\sqrt{2}$. The second column of Fig. 4 shows ρ_{SEEQST} obtained from blockwise reconstruction via SEEQST (blocks are represented with different colors), while the third column displays ρ_{phys} after projection onto the PSD space, ensuring physical validity. The eigenvalues of the unconstrained reconstruction ρ_{SEEQST} are

$$[0.9402, 0.04455, -0.02017, 0.01223, 0.01125, 0.00714, \\ 0.00464, -0.00249, 0.00279, -0.00159, 0.00148, \\ 0.00095, 0.00031, -0.00076, -0.00042, -0.00011],$$

while the eigenvalues of the projected, physically valid density matrix ρ_{phys} are

$$[0.93686, 0.04122, 0.00889, 0.00792, 0.00381, 0.00130, \\ 0, 0, 0, 0, 0, 0, 0, 0, 0].$$

Although ρ_{SEEQST} contains a few negative eigenvalues and is therefore not strictly physical, it nevertheless provides accurate estimates of individual density-matrix elements when compared with both the ideal and PSD-projected states. This demonstrates that even without enforcing positivity constraints, SEEQST can yield reliable and informative reconstructions of the underlying quantum state.

APPENDIX C: SEEQST VERSUS PAULI PARTITIONING

In this Appendix, we describe how and why the SEEQST protocol, and the experiments derived from it, are fundamentally different from the Pauli partitioning protocol, and the experiments derived from that.

A simple and straightforward way to represent and reconstruct an N -qubit density matrix is to expand it in the basis of all 4^N Pauli strings and measure the expectation values of the $4^N - 1$ nonidentity operators. The Pauli partitioning problem focuses on dividing the complete set of N -qubit Pauli operators into subsets containing mutually commuting operators. An optimal partition yields $2^N + 1$ subsets, each containing $2^N - 1$ commuting Pauli operators [68]. Because all operators within a subset commute, they can be measured simultaneously in a single experimental setting, allowing full QST to be completed in just $2^N + 1$ measurement configurations.

However, the measurement settings obtained from Pauli partitioning—though optimal for full-state tomography—do not allow for selective estimation of specific density-matrix

elements, whether individual or grouped. These settings differ fundamentally from those generated by the SEEQST protocol, which are designed explicitly for efficient and direct estimation of targeted elements or blocks. In other words, while data from Pauli-partitioned experiments must be collectively postprocessed (e.g., using maximum-likelihood estimation or similar reconstruction algorithms) to recover the full density matrix, SEEQST experiments directly yield the desired-matrix elements and can also, as a bonus, reconstruct the full density matrix if all measurements are performed.

To make these points more clear, consider the example of two qubits, where the optimal Pauli partitioning (excluding the identity) produces the following five subsets of commuting operators:

$$P_1: \{IX, YI, YX\}, \quad (C1)$$

$$P_2: \{IY, XI, XY\}, \quad (C2)$$

$$P_3: \{IZ, ZI, ZZ\}, \quad (C3)$$

$$P_4: \{XZ, YY, ZX\}, \quad (C4)$$

$$P_5: \{YZ, XX, ZY\}. \quad (C5)$$

Each subset P_i can be measured in a single experimental configuration, so a total of five settings suffices for full QST. However, none of these subsets (except P_3 , which corresponds to the diagonal elements) allows direct estimation of selected off-diagonal density-matrix elements. To recover any specific element or elements, all five measurement settings must be implemented and the measurement data from all subsets must be processed together, yielding the complete density matrix, but without selective or parallel data processing.

In contrast, SEEQST groups density-matrix elements and their corresponding operators as follows:

$$S_1: \{\rho_{00}, \rho_{11}, \rho_{22}, \rho_{33}\} \equiv \{II, IZ, ZI, ZZ\}, \quad (C6)$$

$$S_2: \{\rho_{01}, \rho_{10}, \rho_{23}, \rho_{32}\} \equiv \{IX, IY, ZX, ZY\}, \quad (C7)$$

$$S_3: \{\rho_{02}, \rho_{20}, \rho_{13}, \rho_{31}\} \equiv \{XI, XZ, YI, YZ\}, \quad (C8)$$

$$S_4: \{\rho_{03}, \rho_{12}, \rho_{21}, \rho_{30}\} \equiv \{XX, XY, YX, YY\}. \quad (C9)$$

If, for example, the user is only interested in estimating the elements $\{\rho_{01}, \rho_{23}\} \in S_2$, the relevant operators are $\{IX, IY, ZX, ZY\}$, which can be measured in two experimental settings according to SEEQST. In contrast, under the standard Pauli-partitioning scheme, these operators belong to four different subsets ($IX \in P_1$, $IY \in P_2$, $ZX \in P_4$, $ZY \in P_5$), requiring four separate measurements. Thus, while the complexity of standard Pauli partitioning grows exponentially with the number of qubits and simply lacks selectivity and parallel data-processing features, SEEQST achieves the same goal with a constant, minimal number of experimental settings, independent of system size. Furthermore, SEEQST even allows independent and parallel computation of all subsets S_1, S_2, S_3 , and S_4 , essentially boosting data processing if full QST is desired. Consequently, experiments derived from Pauli partitioning are fundamentally different from what SEEQST gives.

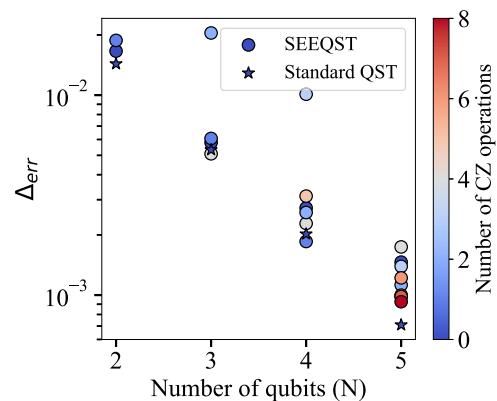


FIG. 5. Average reconstruction error Δ_{err} for N -qubit GHZ states of the form $\frac{1}{\sqrt{2}}(|0\rangle^{\otimes N} - i|1\rangle^{\otimes N})$, as a function of the number of qubits N and the number of CZ operations in the SEEQST circuits.

APPENDIX D: SEEQST OF GHZ STATES

In analogy with the experimental results for the $|+y\rangle^{\otimes N}$ state for systems of up to $N = 5$ qubits, we here present in Fig. 5 the results of QST and SEEQST applied to an initial GHZ state of the form

$$|\psi_{\text{GHZ},N}\rangle = \frac{1}{\sqrt{2}}(|0\rangle^{\otimes N} - i|1\rangle^{\otimes N}). \quad (D1)$$

The average estimation error, Δ_{err} , for each density-matrix element is calculated using Eq. (35). As can be seen in Fig. 5, this error decreases exponentially with the number of qubits, consistent with the trend observed in Fig. 3 for the $|+y\rangle^{\otimes N}$ state. However, somewhat counterintuitively, the error does not increase with the number of CZ gates for GHZ-like states. This deviation occurs because the main source of error is not the gate operations in the measurement circuits, but the inherent imperfections in preparing the GHZ state, which significantly affect the overall error profile.

In Table II, we compare the full state fidelities for the different methods. Due to the dominant readout error of approximately 1% per qubit, standard QST already introduces noticeable noise into the reconstructed state. Nonetheless, the results show that SEEQST achieves fidelities comparable to standard QST, with both methods producing nearly indistinguishable states across all tested qubit numbers.

APPENDIX E: CIRCUIT DEPTH COMPLEXITY IN SEEQST

In this Appendix, we analyze the circuit depth complexity in our SEEQST protocol. Specifically, we consider the implementation of U_{GHZ}^\dagger on an arbitrary subset of M qubits within an N -qubit system.

TABLE II. State fidelity between standard QST, SEEQST, and ideal states for $\frac{1}{\sqrt{2}}(|0\rangle^{\otimes N} - i|1\rangle^{\otimes N})$.

QST comparison \ $N =$	2	3	4	5
Standard and ideal	0.977	0.973	0.966	0.956
SEEQST and ideal	0.983	0.972	0.966	0.953
Standard and SEEQST	0.989	0.985	0.988	0.985

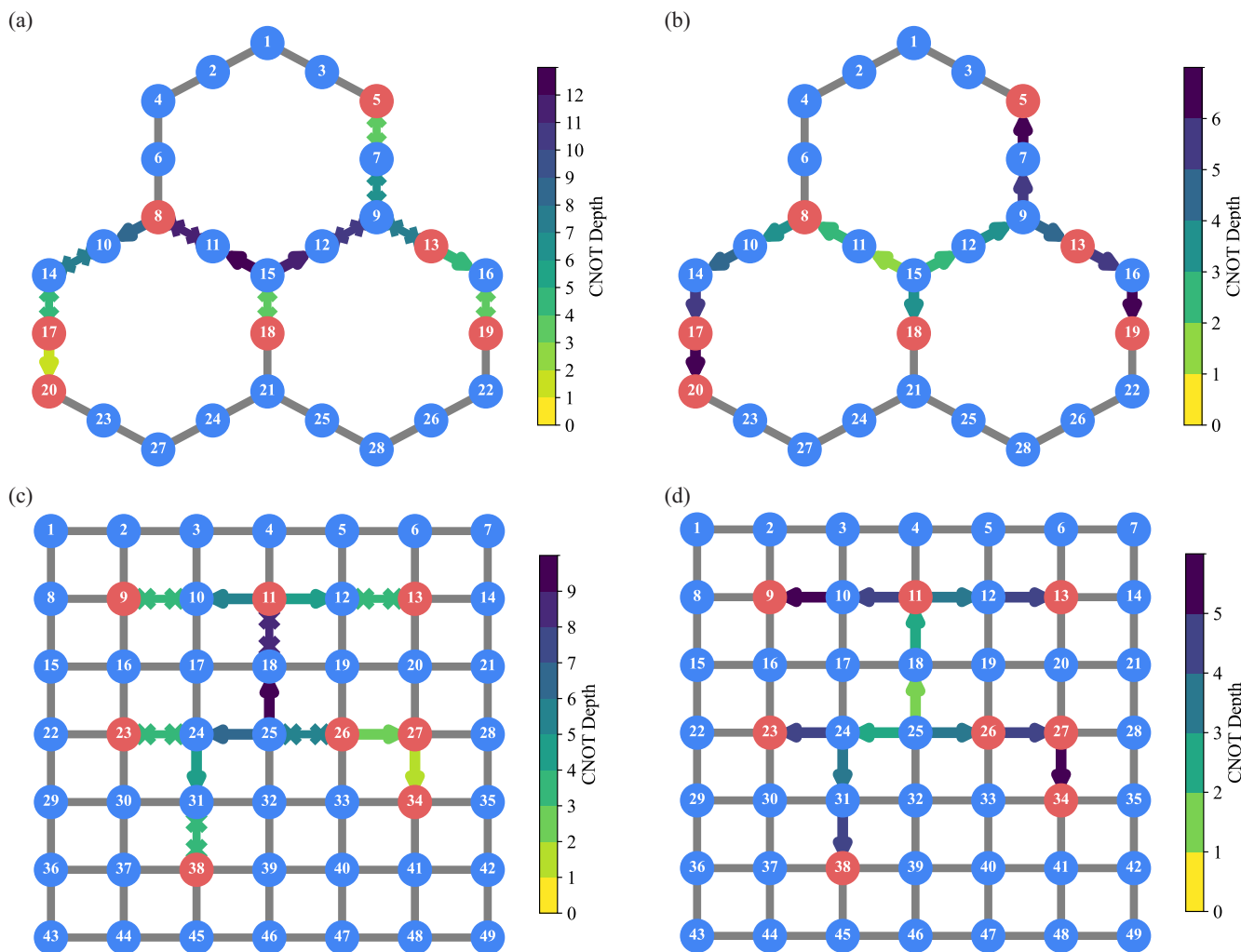


FIG. 6. Circuit depth for SEQST for different qubit layouts. Red nodes represent off-diagonal qubits. Arrows represent CNOT gates (control \rightarrow target), and SWAP gates are denoted by $\times - \times$. (a) Implementation on a heavy-hexagon lattice, inspired by panel (b), which depicts the GHZ-state-generation circuit layout with all red qubits enclosed within boundary B . (c) Implementation on a square lattice, inspired by the GHZ-state-generation layout shown in panel (d).

Figure 2 illustrates a straightforward implementation using a sequential application of $M - 1$ CNOT gates. However, various alternative strategies exist for generating GHZ states across different system layouts, often achieving better depth using parallelization of CNOTs. In an all-to-all connectivity scenario, a GHZ state can be created in $\log_2(M)$ depth by leveraging an entanglement-growing strategy: Once two qubits are entangled, they can be used to entangle two more, then four, and so on.

For a square lattice, optimal parallelization of CNOTs leads to a circuit depth that scales with \sqrt{N} if all N qubits need to be entangled. For an infinite heavy-hexagonal lattice, the optimal circuit depth k is given by [76]

$$k = \left\lceil \frac{\sqrt{8N - 3} - 1}{2} \right\rceil. \tag{E1}$$

Applying U_{GHZ}^\dagger directly in these layouts is straightforward for the fully entangled case, but our goal is to generate a GHZ state only within a selected subset of M qubits, which

may be arbitrarily positioned within the lattice. This constraint necessitates the use of SWAP operations to bring the target qubits into the required locations. However, SWAP gates introduce additional circuit depth. One way to optimize this is by parallelizing SWAP operations, treating them similarly to CNOT gates. Since finding an optimal SWAP sequence is generally an NP-hard problem, we aim to provide an upper bound on circuit depth.

Given an N -qubit lattice with M off-diagonal qubits, this subset lies within the N -qubit layout and has a boundary B . The optimal GHZ generation strategy within this boundary defines the circuit depth k . We can use the reverse path of GHZ generation to reach all M qubits. In particular, since a SWAP gate can be decomposed into three native CNOT gates, the worst-case circuit depth is at most $3k$. We provide some examples of these strategies in Fig. 6, for both heavy-hexagon and square-grid lattices.

Alternative approaches, such as long-range CNOT implementations or GHZ generation via iswap gates, could further optimize the depth. Ultimately, users of SEQST can tailor

TABLE III. Δ_{err} data for the state $|+y\rangle^{\otimes N}$ as illustrated in Fig. 3(b).

No. of CZ gates \ N	2	3	4	5
Standard QST				
0	1.19×10^{-2}	7.09×10^{-3}	3.43×10^{-3}	2.33×10^{-3}
SEEQST				
0	1.64×10^{-2}	9.26×10^{-3}	3.73×10^{-3}	2.03×10^{-3}
1	2.77×10^{-2}	1.12×10^{-2}	6.35×10^{-3}	3.98×10^{-3}
2	–	1.24×10^{-2}	6.86×10^{-3}	2.96×10^{-3}
3	–	1.24×10^{-2}	8.73×10^{-3}	3.59×10^{-3}
4	–	–	4.84×10^{-3}	4.55×10^{-3}
5	–	–	7.37×10^{-3}	4.70×10^{-3}
6	–	–	–	5.07×10^{-3}
7	–	–	–	4.73×10^{-3}
8	–	–	–	4.68×10^{-3}

these methods to their system constraints, as long as they ensure the correct preparation of all eigenstates required by Eqs. (4) and (5).

Note that in our depth calculations, we consider only two-qubit gates, specifically taking CNOT as our baseline metric. We exclude single-qubit gates (including virtual Z gates) since their gate times are significantly shorter and their errors are significantly lower than those for two-qubit operations.

APPENDIX F: EXPERIMENTAL DATA

In Tables III and IV, we present the numerical values for the data points plotted in Figs. 3(b) and 5, respectively.

APPENDIX G: SEEQST USING ONLY SINGLE-QUBIT GATES

In Fig. 2, we employed two-qubit gates to measure all observables in $\mathcal{E}(\Pi^{S_k})$ and $\mathcal{O}(\Pi^{S_k})$ in two separate experiments, utilizing the fact that observables within each set commute globally. To implement SEEQST using only single-qubit gates, the relevant observables must commute locally on each qubit. Using Eq. (28), the circuits required to measure a

given Π^{S_k} can be constructed as follows:

$$\bigotimes_{l=1}^N \begin{cases} I, & \text{if } (i_l, j_l) \in \{(0, 0), (1, 1)\}, \\ \{R_x(\pi/2), R_y(\pi/2)\}, & \text{if } (i_l, j_l) \in \{(0, 1), (1, 0)\}. \end{cases} \tag{G1}$$

If, for a given set, M out of N qubits correspond to odd parity, i.e., $i_k \neq j_k$, then 2^M distinct single-qubit rotation circuits are required to fully access the corresponding observables. Consequently, the optimal (minimal) total number of distinct circuits across all 2^N sets is 3^N in the general case. Therefore, the SEEQST protocol with only single-qubit gates can be regarded as a constrained variant of standard QST, relying solely on local measurement settings and avoiding entangling operations. This approach has been analyzed in Ref. [65].

We analyzed the estimation error Δ_{err} from noiseless simulations of 30 random full-rank density matrices for each $N = 1$ to 6, across varying sample sizes S (number of measurement settings multiplied by number of shots), for both methods. In all cases, the error exhibited the expected $1/\sqrt{S}$ scaling. Additionally, we observed a systematic dependence of the error on the odd-parity index M .

TABLE IV. Δ_{err} data for the state $\frac{1}{\sqrt{2}}(|0\rangle^{\otimes N} - |1\rangle^{\otimes N})$ as illustrated in Fig. 5.

No. of CZ gates \ N	2	3	4	5
Standard QST				
0	1.43×10^{-2}	8.53×10^{-3}	2.02×10^{-3}	7.09×10^{-4}
SEEQST				
0	1.67×10^{-2}	7.58×10^{-3}	2.77×10^{-3}	1.46×10^{-3}
1	1.88×10^{-2}	1.12×10^{-2}	2.83×10^{-3}	8.95×10^{-4}
2	–	2.04×10^{-2}	2.85×10^{-3}	1.32×10^{-3}
3	–	–	1.01×10^{-2}	1.39×10^{-3}
4	–	1.24×10^{-2}	3.13×10^{-3}	2.10×10^{-3}
5	–	–	–	1.62×10^{-3}
6	–	–	–	1.21×10^{-3}

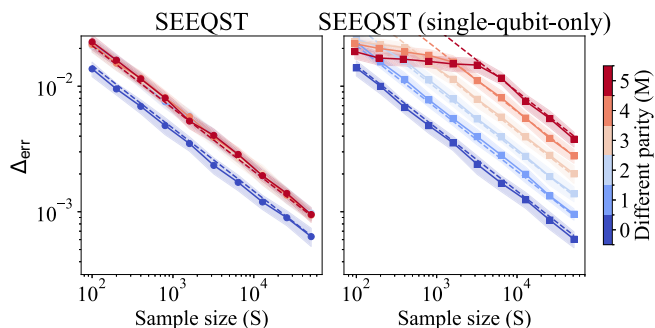


FIG. 7. Mean estimation error Δ_{err} (with standard deviation shaded) as a function of sample size for the SEEQST protocol on a five-qubit system. The figure demonstrates the statistical advantage of using entangled two-qubit gates compared to implementations only employing single-qubit gates, in terms of the number of copies S of the quantum state ρ required. For SEEQST with two-qubit gates, estimation performance remains consistent across different block parities M , except for the diagonal block. In contrast, when restricted to single-qubit gates, the estimation error increases with M , indicating degraded scaling. The fitted empirical scaling relation in Eqs. (G2)–(G4) (dashed lines) captures the observed behavior within standard deviation, except for with very small sample sizes for higher M .

For single-qubit-only SEEQST, the error increases with increasing M , and the error curves appear nearly equally spaced in log scale across different M values, suggesting exponential dependence on M as shown in Fig. 7.

To capture these features, we adopt the following empirical model for single-qubit-only SEEQST:

$$\Delta_{\text{err}}^{\text{SQ}}(N, M) = \frac{2^{A(N)+B(N)\cdot M}}{\sqrt{S}}, \quad (\text{G2})$$

where the functions $A(N)$ and $B(N)$ capture the system-size dependence. We found that power-law forms for both were sufficient to fit the observed behavior within the standard deviation of the data (except for the case of high M with small sample sizes):

$$A(N) = a_0 + a_1 \times N^{a_2}, \quad B(N) = b_1 \times N^{b_2}, \quad (\text{G3})$$

with fitted coefficients

$$a_0 = -0.9177, \quad a_1 = -0.24734, \quad a_2 = 1.2529, \\ b_1 = 0.6358, \quad b_2 = -0.1168.$$

In contrast, our SEEQST protocol employing entangling CNOT gates shows no such dependence on $M \geq 1$. Its estimation error is empirically related to the single-qubit

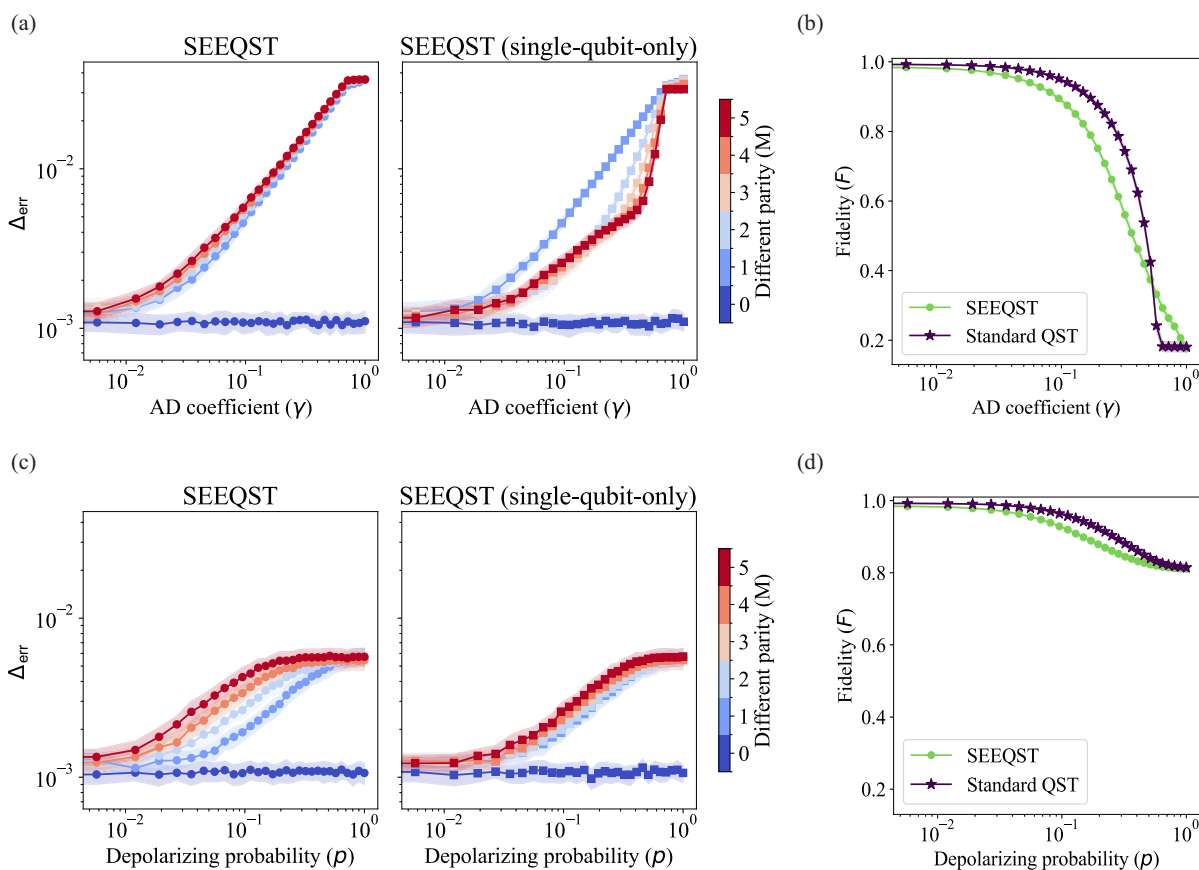


FIG. 8. Numerical simulation of SEEQST performance under noise. The effect of (a) amplitude damping and (c) depolarizing noise on the estimation error Δ_{err} for different SEEQST subsets, categorized by the different parity M . Left panels show results for the standard SEEQST protocol, while right panels show the performance for its single-qubit gates only variant. (b), (d) Impact of amplitude damping and depolarizing noise on the state fidelity F , comparing SEEQST with standard QST. All simulations are for full-rank five-qubit states and 16 384 shots per measurement setting. Solid lines represent the mean over multiple simulation runs, and the shaded regions show the standard deviation.

model as

$$\Delta_{\text{err}}^{\text{CNOT}}(N, M) = \begin{cases} \Delta_{\text{err}}^{\text{SQ}}(N, M = 1), & \text{for } M \geq 1, \\ \Delta_{\text{err}}^{\text{SQ}}(N, M = 0), & \text{for } M = 0. \end{cases} \quad (\text{G4})$$

This highlights the statistical advantage of utilizing entangling gates in SEEQST.

APPENDIX H: NUMERICAL SIMULATION

To systematically evaluate the performance of SEEQST in noisy environments, we conducted numerical simulations on full-rank five-qubit states, using two standard noise models: amplitude damping and depolarizing noise. In each case, noise was introduced by applying errors with a given probability or coefficient after every layer of parallel gates in the measurement circuits. All results were obtained using 16 384 shots per experiment, with state reconstruction performed via a gradient-descent algorithm, as described in the main text. The results are summarized in Fig. 8.

We see from the left panels in Figs. 8(a) and 8(c) that, in the case of standard SEEQST, the estimation error Δ_{err} depends more strongly on the parity parameter M under depolarizing noise than in the presence of amplitude damping. From the right panels in Figs. 8(a) and 8(c), we further observe that the opposite is the case for Δ_{err} in single-qubit-only SEEQST; here, the dependence on M is stronger with amplitude damping than with depolarizing noise. Overall, the standard SEEQST protocol is more noise-sensitive than its single-qubit-only variant, highlighting that while entangling circuits offer a statistical advantage, they are also more susceptible to noise. In terms of overall performance, the state fidelity of SEEQST is slightly lower than that for standard QST under both amplitude damping and depolarizing noise, as shown in Figs. 8(b) and 8(d).

As described in the main text, we employ two approaches for reconstructing the density matrix: (1) maximum-likelihood estimation with Cholesky decomposition and gradient-descent optimization over the full parameter space of the density matrix, and (2) direct estimation, where expectation values $\langle P_i \rangle$ of Pauli observables are estimated using measured population frequencies as probabilities for the

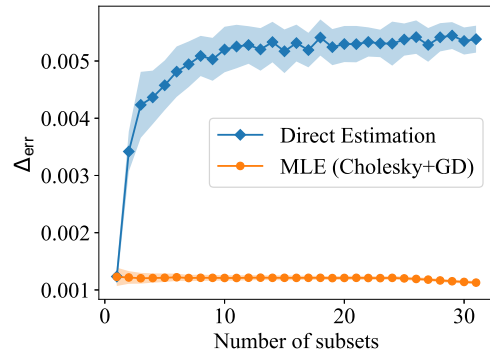


FIG. 9. Δ_{err} as a function of the number of non-diagonal Pauli subsets involved in the reconstruction, averaged over 30 randomly generated full-rank five-qubit states using simulated (16 384 shots per setting). Maximum-likelihood estimation with Cholesky decomposition and gradient descent (GD) maintains a stable error across subset counts due to CPTP constraints, whereas direct estimation shows increasing Δ_{err} with more subsets.

relevant subset of observables. While direct estimation is significantly more computationally efficient, taking on average 10^{-4} s per state on a standard quadcore CPU compared to 0.3 s for MLE for five-qubit states, it exhibits critical limitations. Figure 9 illustrates this drawback.

We compute Δ_{err} across 30 randomly sampled full-rank quantum states for varying numbers of randomly selected subsets (excluding the diagonal subset due to its trivial nature and distinct sample-size scaling). For each number of subsets involved, results are averaged over ten random selections. The plot shows that while the error for MLE remains nearly constant with increasing subsets due to the enforcement of complete positivity and trace preservation (CPTP), direct estimation matches MLE performance only for a single subset and deteriorates quickly as more subsets are included. Although this analysis uses simulated data with 16 384 shots, the effect is expected to be stronger in experiments, where additional noise sources exist. Indeed, as we observed in our IBM hardware experiments, direct estimation exhibited deviations from MLE even when applied to a single subset.

-
- [1] D. F. V. James, P. G. Kwiat, W. J. Munro, and A. G. White, Measurement of qubits, *Phys. Rev. A* **64**, 052312 (2001).
 - [2] M. Paris and J. Řeháček, *Quantum State Estimation*, Lecture Notes in Physics (Springer, Berlin, 2004), Vol. 649.
 - [3] Y.-X. Liu, L. F. Wei, and F. Nori, Tomographic measurements on superconducting qubit states, *Phys. Rev. B* **72**, 014547 (2005).
 - [4] A. I. Lvovsky and M. G. Raymer, Continuous-variable optical quantum-state tomography, *Rev. Mod. Phys.* **81**, 299 (2009).
 - [5] T. Baumgratz, D. Gross, M. Cramer, and M. B. Plenio, Scalable reconstruction of density matrices, *Phys. Rev. Lett.* **111**, 020401 (2013).
 - [6] V. Gebhart, R. Santagati, A. A. Gentile, E. M. Gauger, D. Craig, N. Ares, L. Banchi, F. Marquardt, L. Pezzè, and C. Bonato, Learning quantum systems, *Nat. Rev. Phys.* **5**, 141 (2023).
 - [7] A. Hashim, L. B. Nguyen, N. Goss, B. Marinelli, R. K. Naik, T. Chistolini, J. Hines, J. P. Marceaux, Y. Kim, P. Gokhale, T. Tomesh, S. Chen, L. Jiang, S. Ferracin, K. Rudinger, T. Proctor, K. C. Young, R. Blume-Kohout, and I. Siddiqi, A practical introduction to benchmarking and characterization of quantum computers, *PRX Quantum* **6**, 030202 (2025).
 - [8] R. Blume-Kohout, T. Proctor, and K. Young, Quantum characterization, verification, and validation, [arXiv:2503.16383](https://arxiv.org/abs/2503.16383).
 - [9] C. A. Riofrío, D. Gross, S. T. Flammia, T. Monz, D. Nigg, R. Blatt, and J. Eisert, Experimental quantum compressed sensing for a seven-qubit system, *Nat. Commun.* **8**, 15305 (2017).
 - [10] J. Li, S. Huang, Z. Luo, K. Li, D. Lu, and B. Zeng, Optimal design of measurement settings for quantum-state-tomography experiments, *Phys. Rev. A* **96**, 032307 (2017).

- [11] J. Cotler and F. Wilczek, Quantum overlapping tomography, *Phys. Rev. Lett.* **124**, 100401 (2020).
- [12] Z. Hradil, Quantum-state estimation, *Phys. Rev. A* **55**, R1561 (1997).
- [13] K. Banaszek, G. M. D'Ariano, M. G. A. Paris, and M. F. Sacchi, Maximum-likelihood estimation of the density matrix, *Phys. Rev. A* **61**, 010304(R) (1999).
- [14] A. I. Lvovsky, Iterative maximum-likelihood reconstruction in quantum homodyne tomography, *J. Opt. B: Quantum Semiclassical Opt.* **6**, S556 (2004).
- [15] J. Řeháček, Z. Hradil, E. Knill, and A. I. Lvovsky, Diluted maximum-likelihood algorithm for quantum tomography, *Phys. Rev. A* **75**, 042108 (2007).
- [16] J. A. Smolin, J. M. Gambetta, and G. Smith, Efficient method for computing the maximum-likelihood quantum state from measurements with additive gaussian noise, *Phys. Rev. Lett.* **108**, 070502 (2012).
- [17] J. Shang, Z. Zhang, and H. K. Ng, Superfast maximum-likelihood reconstruction for quantum tomography, *Phys. Rev. A* **95**, 062336 (2017).
- [18] C. Ferrie, Self-guided quantum tomography, *Phys. Rev. Lett.* **113**, 190404 (2014).
- [19] E. Bolduc, G. C. Knee, E. M. Gauger, and J. Leach, Projected gradient descent algorithms for quantum state tomography, *npj Quantum Inf.* **3**, 44 (2017).
- [20] M.-C. Hsu, E.-J. Kuo, W.-H. Yu, J.-F. Cai, and M.-H. Hsieh, Quantum state tomography via nonconvex riemannian gradient descent, *Phys. Rev. Lett.* **132**, 240804 (2024).
- [21] Y. Wang, L. Liu, S. Cheng, L. Li, and J. Chen, Efficient factored gradient descent algorithm for quantum state tomography, *Phys. Rev. Res.* **6**, 033034 (2024).
- [22] A. Gaikwad, M. S. Torres, S. Ahmed, and A. F. Kockum, Gradient-descent methods for fast quantum state tomography, *Quantum Sci. Technol.* **10**, 045055 (2025).
- [23] D. Hoshi, T. Nagase, S. Kwon, D. Iyama, T. Kamiya, S. Fujii, H. Mukai, S. Ahmed, A. F. Kockum, S. Watabe, F. Yoshihara, and J.-S. Tsai, Entangling Schrödinger's cat states by bridging discrete- and continuous-variable encoding, *Nat. Commun.* **16**, 1309 (2025).
- [24] Y. Quek, S. Fort, and H. K. Ng, Adaptive quantum state tomography with neural networks, *npj Quantum Inf.* **7**, 105 (2021).
- [25] S. Lohani, B. T. Kirby, M. Brodsky, O. Danaci, and R. T. Glasser, Machine learning assisted quantum state estimation, *Mach. Learn.: Sci. Technol.* **1**, 035007 (2020).
- [26] A. Gaikwad, O. Bihani, Arvind, and K. Dorai, Neural-network-assisted quantum state and process tomography using limited data sets, *Phys. Rev. A* **109**, 012402 (2024).
- [27] T. Schmale, M. Reh, and M. Gärtner, Efficient quantum state tomography with convolutional neural networks, *npj Quantum Inf.* **8**, 115 (2022).
- [28] S. Ahmed, C. Sánchez Muñoz, F. Nori, and A. F. Kockum, Quantum state tomography with conditional generative adversarial networks, *Phys. Rev. Lett.* **127**, 140502 (2021).
- [29] S. Ahmed, C. Sánchez Muñoz, F. Nori, and A. F. Kockum, Classification and reconstruction of optical quantum states with deep neural networks, *Phys. Rev. Res.* **3**, 033278 (2021).
- [30] S. Yu, F. Albarrán-Arriagada, J. C. Retamal, Y.-T. Wang, W. Liu, Z.-J. Ke, Y. Meng, Z.-P. Li, J.-S. Tang, E. Solano, L. Lamata, C.-F. Li, and G.-C. Guo, Reconstruction of a photonic qubit state with reinforcement learning, *Adv. Quantum Technol.* **2**, 1800074 (2019).
- [31] N. Innan, O. I. Siddiqui, S. Arora, T. Ghosh, Y. P. Koçak, D. Paragas, A. A. O. Galib, M. A.-Z. Khan, and M. Bennai, Quantum state tomography using quantum machine learning, *Quantum Mach. Intell.* **6**, 28 (2024).
- [32] T. Xin, X. Nie, X. Kong, J. Wen, D. Lu, and J. Li, Quantum pure state tomography via variational hybrid quantum-classical method, *Phys. Rev. Appl.* **13**, 024013 (2020).
- [33] Y. Liu, D. Wang, S. Xue, A. Huang, X. Fu, X. Qiang, P. Xu, H.-L. Huang, M. Deng, C. Guo, X. Yang, and J. Wu, Variational quantum circuits for quantum state tomography, *Phys. Rev. A* **101**, 052316 (2020).
- [34] D. Gross, Y.-K. Liu, S. T. Flammia, S. Becker, and J. Eisert, Quantum state tomography via compressed sensing, *Phys. Rev. Lett.* **105**, 150401 (2010).
- [35] A. Steffens, C. A. Riofrafrao, W. McCutcheon, I. Roth, B. A. Bell, A. McMillan, M. S. Tame, J. G. Rarity, and J. Eisert, Experimentally exploring compressed sensing quantum tomography, *Quantum Sci. Technol.* **2**, 025005 (2017).
- [36] I. Strandberg, Simple, reliable, and noise-resilient continuous-variable quantum state tomography with convex optimization, *Phys. Rev. Appl.* **18**, 044041 (2022).
- [37] A. Gaikwad, Arvind, and K. Dorai, True experimental reconstruction of quantum states and processes via convex optimization, *Quantum Inf. Proc.* **20**, 19 (2021).
- [38] R. Nehra, M. Eaton, C. González-Arciniegas, M. S. Kim, T. Gerrits, A. Lita, S. W. Nam, and O. Pfister, Generalized overlap quantum state tomography, *Phys. Rev. Res.* **2**, 042002(R) (2020).
- [39] M. Cramer, M. B. Plenio, S. T. Flammia, R. Somma, D. Gross, S. D. Bartlett, O. Landon-Cardinal, D. Poulin, and Y.-K. Liu, Efficient quantum state tomography, *Nat. Commun.* **1**, 149 (2010).
- [40] B. P. Lanyon, C. Maier, M. Holzäpfel, T. Baumgratz, C. Hempel, P. Jurcevic, I. Dhand, A. S. Buyskikh, A. J. Daley, M. Cramer, M. B. Plenio, R. Blatt, and C. F. Roos, Efficient tomography of a quantum many-body system, *Nat. Phys.* **13**, 1158 (2017).
- [41] G. Tóth, W. Wieczorek, D. Gross, R. Krischek, C. Schwemmer, and H. Weinfurter, Permutationally invariant quantum tomography, *Phys. Rev. Lett.* **105**, 250403 (2010).
- [42] A. Kyriillidis, A. Kalev, D. Park, S. Bhojanapalli, C. Caramanis, and S. Sanghavi, Provable compressed sensing quantum state tomography via non-convex methods, *npj Quantum Inf.* **4**, 36 (2018).
- [43] S. T. Flammia and Y.-K. Liu, Direct fidelity estimation from few pauli measurements, *Phys. Rev. Lett.* **106**, 230501 (2011).
- [44] H.-Y. Huang, R. Kueng, and J. Preskill, Predicting many properties of a quantum system from very few measurements, *Nat. Phys.* **16**, 1050 (2020).
- [45] S. N. Hearsh, M. O. Flynn, A. Chandran, and C. R. Laumann, Efficient local classical shadow tomography with number conservation, *Phys. Rev. Lett.* **133**, 060802 (2024).
- [46] X. Bonet-Monroig, R. Babbush, and T. E. O'Brien, Nearly optimal measurement scheduling for partial tomography of quantum states, *Phys. Rev. X* **10**, 031064 (2020).
- [47] J. S. Lundeen and C. Bamber, Procedure for direct measurement of general quantum states using weak measurement, *Phys. Rev. Lett.* **108**, 070402 (2012).

- [48] S. Wu, State tomography via weak measurements, *Sci. Rep.* **3**, 1193 (2013).
- [49] A. Gaikwad, G. Singh, K. Dorai, and Arvind, Direct tomography of quantum states and processes via weak measurements of Pauli spin operators on an NMR quantum processor, *Eur. Phys. J. D* **77**, 209 (2023).
- [50] Y. Kim, Y.-S. Kim, S.-Y. Lee, S.-W. Han, S. Moon, Y.-H. Kim, and Y.-W. Cho, Direct quantum process tomography via measuring sequential weak values of incompatible observables, *Nat. Commun.* **9**, 192 (2018).
- [51] L. Calderaro, G. Foletto, D. Dequal, P. Villorosi, and G. Vallone, Direct reconstruction of the quantum density matrix by strong measurements, *Phys. Rev. Lett.* **121**, 230501 (2018).
- [52] G. S. Thekkadath, L. Giner, Y. Chalich, M. J. Horton, J. Banker, and J. S. Lundeen, Direct measurement of the density matrix of a quantum system, *Phys. Rev. Lett.* **117**, 120401 (2016).
- [53] S. Zhang, Y. Zhou, Y. Mei, K. Liao, Y.-L. Wen, J. Li, X.-D. Zhang, S. Du, H. Yan, and S.-L. Zhu, δ -quench measurement of a pure quantum-state wave function, *Phys. Rev. Lett.* **123**, 190402 (2019).
- [54] T. Feng, C. Ren, and X. Zhou, Direct measurement of density-matrix elements using a phase-shifting technique, *Phys. Rev. A* **104**, 042403 (2021).
- [55] C. Li, Y. Wang, T. Feng, Z. Li, C. Ren, and X. Zhou, Direct measurement of density-matrix elements with a phase-shifting technique on a quantum photonic chip, *Phys. Rev. A* **105**, 062414 (2022).
- [56] A. K. Ekert, C. M. Alves, D. K. L. Oi, M. Horodecki, P. Horodecki, and L. C. Kwek, Direct estimations of linear and nonlinear functionals of a quantum state, *Phys. Rev. Lett.* **88**, 217901 (2002).
- [57] A. Bendersky and J. P. Paz, Selective and efficient quantum state tomography and its application to quantum process tomography, *Phys. Rev. A* **87**, 012122 (2013).
- [58] E. Bolduc, G. Gariépy, and J. Leach, Direct measurement of large-scale quantum states via expectation values of non-Hermitian matrices, *Nat. Commun.* **7**, 10439 (2016).
- [59] V. Feldman and A. Bendersky, Selective quantum state tomography for continuous-variable systems, *Phys. Rev. A* **105**, 032453 (2022).
- [60] J. Morris and B. Dakić, Selective quantum state tomography, [arXiv:1909.05880](https://arxiv.org/abs/1909.05880).
- [61] V. Feldman and A. Bendersky, Selective continuous-variable quantum process tomography, *Phys. Rev. A* **111**, 042409 (2025).
- [62] H. Laurell, S. Luo, R. Weissenbilder, M. Ammitzböll, S. Ahmed, H. Söderberg, C. Leon, M. Petersson, V. Poulain, C. Guo, C. Dittel, D. Finkelstein-Shapiro, R. J. Squibb, R. Feifel, M. Gisselbrecht, C. L. Arnold, A. Buchleitner, E. Lindroth, A. Frisk Kockum, A. L'Huillier, and D. Busto, Measuring the quantum state of photoelectrons, *Nat. Photon.* **19**, 352 (2025).
- [63] K. He, M. Yuan, Y. Wong, S. Chakram, A. Seif, L. Jiang, and D. I. Schuster, Efficient multimode Wigner tomography, *Nat. Commun.* **15**, 4138 (2024).
- [64] Z. Kis and S. Stenholm, Measuring the density matrix by local addressing, *Phys. Rev. A* **64**, 065401 (2001).
- [65] A. Sengupta, A. Chatterjee, G. J. Sreejith, and T. S. Mahesh, Partial quantum shadow tomography for structured operators and its experimental demonstration using NMR, *Phys. Rev. A* **113**, 032419 (2026).
- [66] D. Goyeneche, G. Cañas, S. Etcheverry, E. S. Gómez, G. B. Xavier, G. Lima, and A. Delgado, Five measurement bases determine pure quantum states on any dimension, *Phys. Rev. Lett.* **115**, 090401 (2015).
- [67] T. Feng, T. Xiao, Y. Wang, S. Pang, F. Hanif, X. Zhou, Q. Zhao, M. S. Kim, and J. Sun, Two measurement bases are asymptotically informationally complete for any pure state tomography, [arXiv:2501.17061v1](https://arxiv.org/abs/2501.17061v1).
- [68] B. Reggiov, N. Butt, A. Lytle, and P. Draper, Fast partitioning of Pauli strings into commuting families for optimal expectation value measurements of dense operators, *Phys. Rev. A* **110**, 022606 (2024).
- [69] E. van den Berg and K. Temme, Circuit optimization of Hamiltonian simulation by simultaneous diagonalization of Pauli clusters, *Quantum* **4**, 322 (2020).
- [70] Python code for SEEQST, <https://github.com/aniket-ae/SEEQST>.
- [71] A. Gaikwad, D. Rehal, A. Singh, Arvind, and K. Dorai, Experimental demonstration of selective quantum process tomography on an NMR quantum information processor, *Phys. Rev. A* **97**, 022311 (2018).
- [72] A. Gaikwad, K. Shende, Arvind, and K. Dorai, Implementing efficient selective quantum process tomography of superconducting quantum gates on IBM quantum experience, *Sci. Rep.* **12**, 3688 (2022).
- [73] D. M. Greenberger, M. A. Horne, and A. Zeilinger, Going beyond Bell's theorem, in *Bell's Theorem, Quantum Theory and Conceptions of the Universe*, edited by M. Kafatos (Springer, Netherlands, 1989), p. 69.
- [74] W. Dür, G. Vidal, and J. I. Cirac, Three qubits can be entangled in two inequivalent ways, *Phys. Rev. A* **62**, 062314 (2000).
- [75] M. Ippoliti, Classical shadows based on locally-entangled measurements, *Quantum* **8**, 1293 (2024).
- [76] J. F. Kam, H. Kang, C. D. Hill, G. J. Mooney, and L. C. L. Hollenberg, Characterization of entanglement on superconducting quantum computers of up to 414 qubits, *Phys. Rev. Res.* **6**, 033155 (2024).
- [77] G. J. Mooney, G. A. L. White, C. D. Hill, and L. C. L. Hollenberg, Generation and verification of 27-qubit Greenberger-Horne-Zeilinger states in a superconducting quantum computer, *J. Phys. Commun.* **5**, 095004 (2021).
- [78] W. Feng, G.-Q. Zhang, Q.-P. Su, J.-X. Zhang, and C.-P. Yang, Generation of Greenberger-Horne-Zeilinger states on two-dimensional superconducting-qubit lattices via parallel multiqubit-gate operations, *Phys. Rev. Appl.* **18**, 064036 (2022).
- [79] H. Liao, G. S. Hartnett, A. Kakkar, A. Tan, M. Hush, P. S. Mundada, M. J. Biercuk, and Y. Baum, Achieving computational gains with quantum error-correction primitives: Generation of long-range entanglement enhanced by error detection, *PRX Quantum* **6**, 020331 (2025).
- [80] *ibm_marrakesh* processor specifications, https://quantum.ibm.com/services/resources?type=Heron&system=ibm_marrakesh.
- [81] R. Jozsa, Fidelity for mixed quantum states, *J. Mod. Opt.* **41**, 2315 (1994).
- [82] D. Binosi, G. Garberoglio, D. Maragnano, M. Dapor, and M. Liscidini, A tailor-made quantum state tomography approach, *APL Quantum* **1**, 036112 (2024).

- [83] M.-D. Choi, Completely positive linear maps on complex matrices, *Linear Algebra Appl.* **10**, 285 (1975).
- [84] D. W. Leung, Choi's proof as a recipe for quantum process tomography, *J. Math. Phys.* **44**, 528 (2003).
- [85] M. Jiang, S. Luo, and S. Fu, Channel-state duality, *Phys. Rev. A* **87**, 022310 (2013).
- [86] M. Cattaneo, M. A. C. Rossi, K. Korhonen, E.-M. Borrelli, G. García-Pérez, Z. Zimborás, and D. Cavalcanti, Self-consistent quantum measurement tomography based on semidefinite programming, *Phys. Rev. Res.* **5**, 033154 (2023).
- [87] J. Barberà-Rodríguez, L. Zambrano, A. Acín, and D. Farina, Boosting projective methods for quantum process and detector tomography, *Phys. Rev. Res.* **7**, 013208 (2025).
- [88] L. Zambrano, S. Ramos-Calderer, and R. Kueng, Fast quantum measurement tomography with dimension-optimal error bounds, [arXiv:2507.04500](https://arxiv.org/abs/2507.04500).